A Journal of the Gesellschaft Deutscher Chemiker
Angewandte Chemie
GDCh
International Edition
www.angewandte.org

Accepted Article

Title: PtSe2/Pt heterointerface with reduced coordination for boosted hydrogen evolution reaction

Authors: Zongpeng Wang, Beibei Xiao, Zhiping Lin, Yaping Xu, Yan Lin, Fanqi Meng, Qinghua Zhang, Lin Gu, Baizeng Fang, Shaojun Guo, and Wenwu Zhong

To be cited as: *Angew. Chem. Int. Ed.* 10.1002/anie.202110335

Link to VoR: https://doi.org/10.1002/anie.202110335

WILEY-VCH

10.1002/anie.202110335

$PtSe_2/Pt$ heterointerface with reduced coordination for boosted hydrogen evolution reaction

Zongpeng Wang[1,+], Beibei Xiao[2,+], Zhiping Lin[1], Yaping Xu[1], Yan Lin[1], Fanqi Meng[3], Qinghua Zhang[3], Lin Gu[3], Baizeng Fang[4], Shaojun Guo[5] and Wenwu Zhong[1,*]

[1]School of Advanced study, Taizhou University, Taizhou, China.

[2]School of Energy and Power Engineering, Jiangsu University of Science and Technology, Zhenjiang, China.

[3]Institution of Physics, Chinese Academic of Science, Beijing, China.

[4]Department of Chemical & Biological Engineering, University of British Columbia, 2360 East Mall, Vancouver, BC V6T 1Z3, Canada..

[5]School of Materials Science and Engineering, Peking University, Beijing, China.

[*]zhongww@tzc.edu.cn

[+]These authors contribute equally to this work.

Abstract

$PtSe_2$ is a typical noble metal dichalcogenide (NMD) that holds promising possibility for next-generation electronics and photonics. However, when applied in hydrogen evolution reaction (HER), it exhibits sluggish kinetics due to the insufficient capability of absorbing active species. Here, we construct $PtSe_2/Pt$ heterointerface to boost the reaction dynamics of $PtSe_2$, enabled by an in-situ electrochemical method. It is found that Se vacancies are induced around the heterointerface, reducing the coordination environment. Correspondingly, the exposed Pt atoms at the very vicinity of Se vacancies are activated, with enhanced overlap with H 1s orbital. The adsorption of $H^{\bullet}$ intermediate is thus strengthened, achieving near thermoneutral free energy change. Consequently, the as-prepared $PtSe_2/Pt$ exhibits extraordinary HER activity even superior to Pt/C, with an overpotential of 42 mV at 10 mA/cm^2 and a Tafel slope of 53 mV/dec. This work raises attention on NMDs toward HER and provides insights for the rational construction of novel heterointerfaces.

Keywords: Hydrogen evolution reaction, noble metal dichalcogenides, heterointerface

1. Introduction

Noble metal dichalcogenides (NMDs) are attracting wide attentions as a novel group in the 2D material family, due to their high carrier mobility, tunable bandgap and excellent stability[1]. Adopting NMDs in electrocatalysis holds promising prospects[2]. For transition metals compounds, the d-electrons define the phase structure, the coordination environment and the resulting interaction strength with active species[3]. Notably, the d-bands are highly occupied in NMDs, offering a unique platform for the research of regulative electrocatalytic activity. For example, Hu et al. studied the layer dependent HER (hydrogen evolution reaction) performance of $PtSe_2$ nanosheets, and found that the activity raised monotonically with increasing layer number[4]. Lin et al. fabricated vertically stacked $PtSe_2$ nanosheets through selenization of magnetron sputtering Pt film to enlarge the edge density for optimized HER activity[5]. However, as demonstrated by these works, the HER performance of $PtSe_2$ is considerably low.

Constructing heterointerface is powerful strategy to design high-performance materials, where exceptional phenomenon and physics can be observed, including band bending[6], charge redistribution[7], phase transaction[8] and so on. In electrocatalytic HER, the density of active sites and the intrinsic activity are two vital factors that define the efficiency of a catalyst[9]. Engineering suitable heterointerfaces can not only regulate the morphology of materials, increasing active sites loading, but also can modulate the electronic structure and optimize the adsorption behavior, enhancing the intrinsic activity. For example, Zhu et al. used eutectic salt system to fabricate Ru/RuS_2 heterointerface, where the electronic state and charge distribution were regulated to achieve optimized adsorption behavior with a resulting overpotential of 45 mV at 10 mA cm^{-2} in acidic media[10]. Despite the numerous reports on various heterointerface forms, the effect of innovative vacancies that induced by the construction of heterointerfaces is rarely explored.

In this work, to boost the HER activity of $PtSe_2$ and demonstrate the versatile capability of heterointerfaces, we constructed $PtSe_2/Pt$ interface through an electrochemical reduction method, where tremendous Pt ultra-small particles are generated at the edges of $PtSe_2$ nanosheets. It is revealed that continuous Se vacancies are induced around the $PtSe_2/Pt$ boundary, resulting in reduced coordination environment. Benefitting from this unique structure, the adsorption of $H^\bullet$ intermediate on this material is strengthened compared to the otherwise insufficient adsorption, achieving optimal thermoneutral free energy change. Besides, the combination of Pt can effectively improve the electrical conductivity of the material. Consequently, the as-prepared $PtSe_2/Pt$ exhibits extraordinary HER activity even superior to Pt/C, with an overpotential of 42 mV at 10 mA/cm^2

10.1002/anie.202110335

and a Tafel slope of 53 mV/dec.

2. Results and discussion

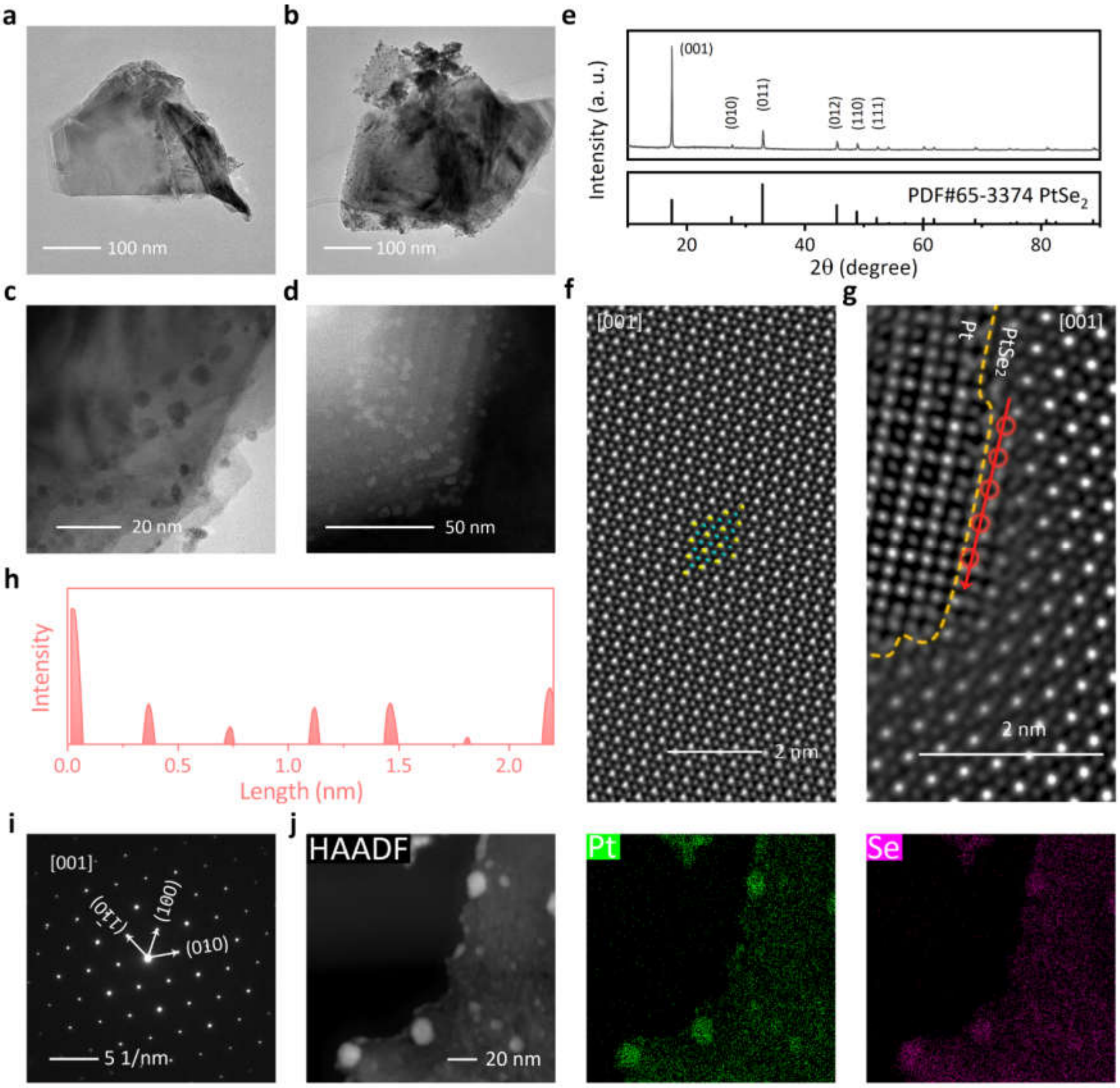

Figure 1. Morphology and crystal structure. **a,b** TEM images of $PtSe_2$ and $PtSe_2$/Pt, respectively. **c,d** Magnified TEM and STEM image of $PtSe_2$/Pt, respectively. **e** XRD pattern of $PtSe_2$/Pt. Vertical black lines are used to represent the information of the standard PDF card. **f** HAADF-STEM image of the $PtSe_2$ sheet in $PtSe_2$/Pt sample, viewed from [001] direction Inset: overlap of corresponding $PtSe_2$ lattice with yellow dots representing Pt atoms and blue dots representing Se atoms. **g** HAADF-STEM image of the boundary between $PtSe_2$ sheet and Pt cluster in $PtSe_2$/Pt. **h** The intensity profile along the red-arrow line in g. **i** SEAD pattern of $PtSe_2$/Pt. **j** Element mapping of $PtSe_2$/Pt.

The morphology and structure of the prepared samples were characterized, shown in Figure 1 and Figure S1. The TEM images of $PtSe_2$ and $PtSe_2$/Pt are shown in Figure 1 a and b, respectively. $PtSe_2$ nanosheets exhibit layered crystal structure, which can be reflected by the fringes at the edges of the sample in Figure 1a. In the TEM image of $PtSe_2$/Pt, one can see clearly that tremendous ultra-small Pt particles were loaded on $PtSe_2$ nanosheets. To examine the distribution of ultra-small Pt particles more distinctly, the enlarged TEM and STEM (scanning TEM) image of $PtSe_2$/Pt were captured in Figure 1 c and d, respectively. As one can see, the ultra-small Pt particles were distributed along the edges of $PtSe_2$ nanosheets. This unique distribution of ultra-small Pt particles not only increases the electrical conductivity of $PtSe_2$/Pt sample, but also modulates the local structure of $PtSe_2$/Pt, forming highly active sites for HER. Figure 1e presents the XRD (X-ray diffraction) pattern of the sample, which matches well with the standard peaks of $PtSe_2$ (PDF card No. 65-3374, Table S1). The first six peaks located at 17°, 28°, 33°, 45°, 49° and 52° correspond to the (001), (010), (011), (012), (110) and (111) facets of $PtSe_2$, respectively. The strongest peak is different from the standard PDF card, which is due to the layered structure of $PtSe_2$. The dominate (001) peak is also observed in many 2D materials. Note that the XRD patterns of Pt are invisible due to the extremely low mass ratio of ultra-small Pt particles. The presence of Pt is evidenced by more surface-sensitive characterizations in the following. To further explore the structure of the prepared $PtSe_2$/Pt sample, Figure 1 f and g display the HAADF-STEM (high angle annular dark filed STEM) images of $PtSe_2$/Pt sample at the basal plane and the boundary, respectively. The brighter and bigger spots represent the heavier Pt atoms, while the darker and smaller spots are Se atoms. Figure 1f matches exactly with the [001] facets of $PtSe_2$ crystal, indicating the successful preparation of the desired sample. Figure 1g depicts a typical boundary area between $PtSe_2$ nanosheet and Pt cluster. It is worthy to note that Se vacancies appear at the very close neighbor along the boundary. The intensity distribution of Se signal along the red arrow is shown in Figure 1h. One can see the Se signal decreases obviously at the vacancy positions. The SAED (selected area electron diffraction) pattern of the prepared $PtSe_2$/Pt sample is shown in Figure 1i, which can be indexed to diffraction along [001] direction. Corresponding facets in the diffraction parallelogram are marked. Figure 1j presents the element mapping of the $PtSe_2$/Pt sample. One can see the Pt signal is much brighter with the appearance of the ultra-small Pt particles, indicating the chemical nature of the observed particles.

10.1002/anie.202110335

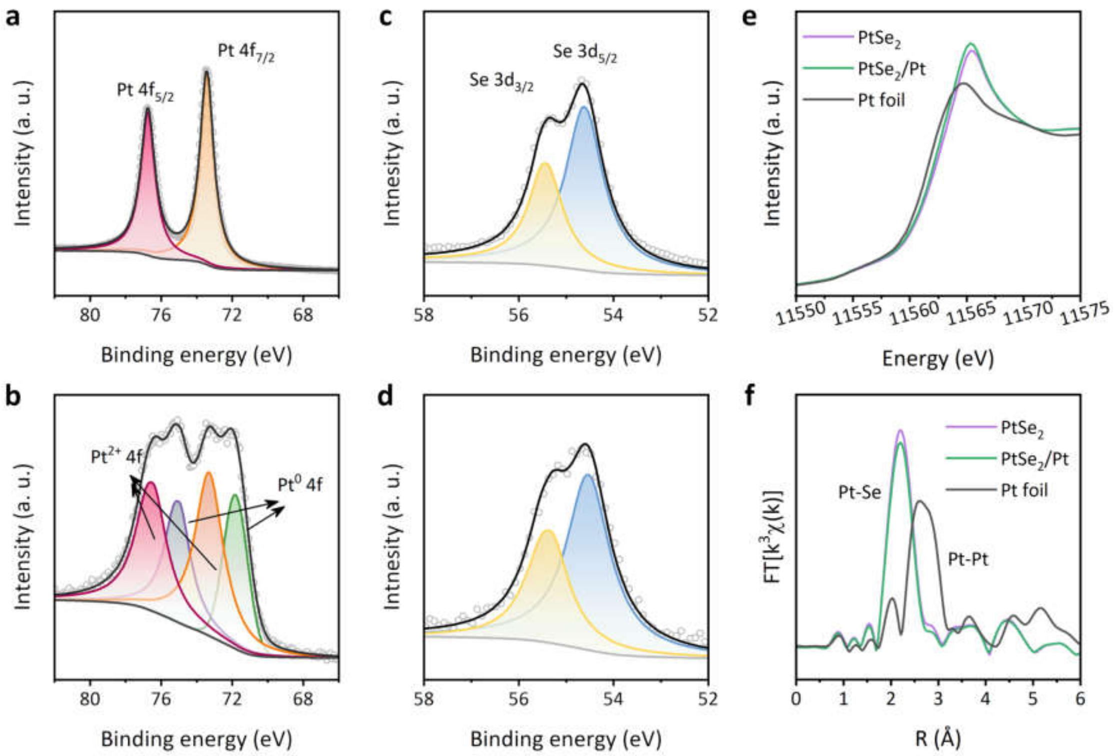

Figure 2. Oxidation state of $PtSe_2$/Pt. **a,b** High-resolution XPS spectra of Pt 4f orbitals of $PtSe_2$ and $PtSe_2$/Pt, respectively. **c,d** High-resolution XPS spectra of Se 3d orbitals of $PtSe_2$ and $PtSe_2$/Pt, respectively. **e** XANES of corresponding samples. **f** EXAFS of corresponding samples.

The valence state and chemical coordination environment of the prepared samples were characterized by XPS (X-ray photoelectron spectroscopy) and XAS (X-ray absorption spectroscopy). The XPS spectra were calibrated using the C1s peak (Figure S2). Figure 2a and Figure 2b compare the high-resolution XPS spectra of Pt 4f orbitals of $PtSe_2$ and $PtSe_2$/Pt, respectively. The deconvoluted peaks located at around 76 and 72.6 eV correspond to the $4f_{5/2}$ and $4f_{7/2}$ orbitals of Pt^{2+}, respectively, which is in consistent with references[11]. It is observed that another pair of peaks emerges for the $PtSe_2$/Pt sample, located at 74.4 and 71.1 eV. These peaks correspond to the $4f_{5/2}$ and $4f_{7/2}$ orbitals of Pt^0, respectively, reflecting the presence of ultra-small Pt particles. We noticed the formula of $PtSe_2$ indicates a +4 valence of Pt. However, based on the comparison of the binding energy of Pt in different oxides[12], the peaks around 76 and 72.6 eV belong to the doublets of Pt^{2+} state. Therefore, we believe Pt in $PtSe_2$ should exhibit a +2 valence. The high-resolution XPS spectra of Se 3d orbitals of $PtSe_2$ and $PtSe_2$/Pt are displayed in Figure 2c and Figure 2d, respectively. The peaks located at 55 and 54.1 eV correspond to Se $3d_{3/2}$ and $3d_{5/2}$ orbitals, respectively[13]. Figure 2e presents the XANES (X-ray absorption near edge structure) of

10.1002/anie.202110335

samples with various valence states of Pt. The absorption edges originate from the Pt L_3 electron transaction. One can see the absorption edge of $PtSe_2$/Pt locates between Pt foil and $PtSe_2$ samples, indicating the valence state of Pt in $PtSe_2$/Pt is between 0 and +2. This is because the generation of Pt cluster at the edges of $PtSe_2$ nanosheets. Figure 2f and Figure S3 show the EXAFS (extended X-ray absorption fine structure) of corresponding samples. The characteristic peak at 2.6 Å stands for Pt-Pt coordination, while the peak at 2.2 Å stands for Pt-Se coordination. The presence of ultra-small Pt particles could also be reflected by the reduced Pt-Se coordination in $PtSe_2$/Pt, compared to $PtSe_2$.

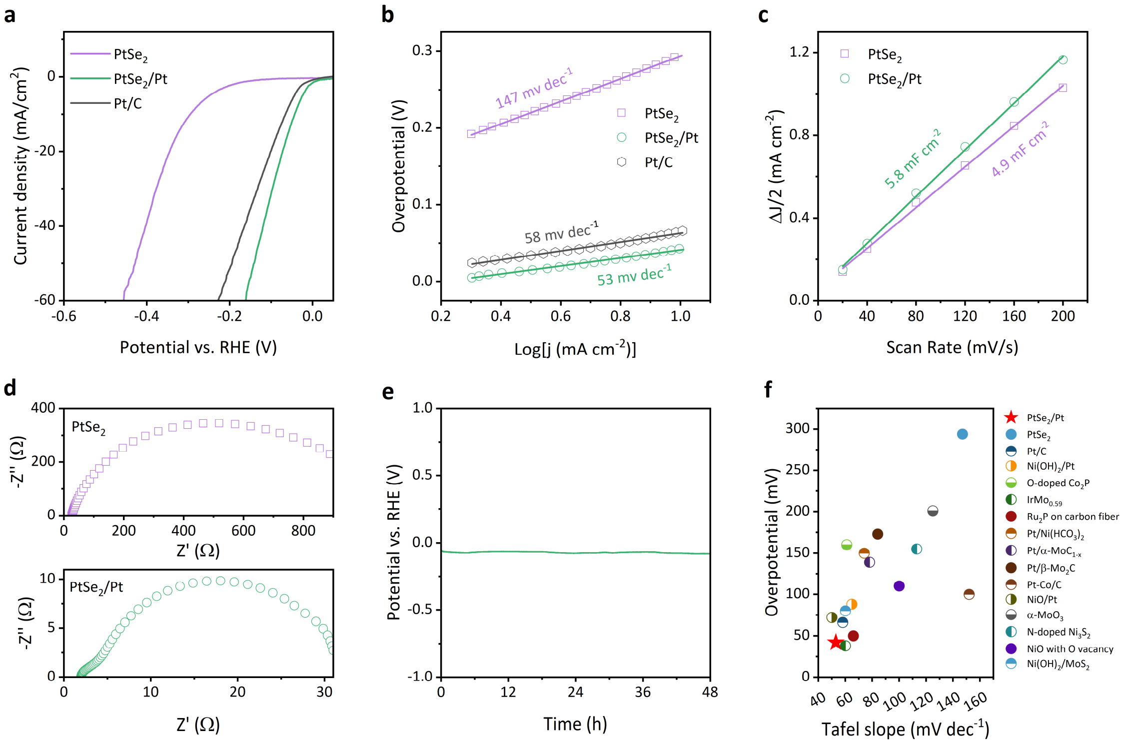

Figure 3. Electrochemical measurements of the prepared samples for HER. **a** iR-corrected linear sweep polarization curves in 1 M KOH. **b** Corresponding Tafel slopes. **c** Derived double layer capacitance Cdl. **d** Electrochemical impedance diagrams of $PtSe_2$ and $PtSe_2$/Pt samples, respectively. **e** Stability test at 10 mA cm^{-2}. **f** Comparison of the Tafel slope and overpotential for various Pt-based or typical HER catalysts in alkaline electrolyte, with data extracted from references[14].

The HER activity of $PtSe_2$/Pt is evaluated in 1 M KOH, with results shown in Figure 3. The iR-corrected linear sweep voltammetry of the prepared samples is shown in Figure 3a. As one can see in Figure 3a and Figure 3b, the $PtSe_2$ nanosheet exhibits an overpotential of 294 mV at 10 mA/cm^2

10.1002/anie.202110335

and a Tafel slope of 147 mV/dec, while those of $PtSe_2/Pt$ sample are 42 mV and 53 mV/dec, respectively. The HER activity of $PtSe_2/Pt$ is far superior to that of $PtSe_2$. More importantly, $PtSe_2/Pt$ performs even better than Pt/C electrode (with an overpotential of 65 mV at 10 mA/cm^2 and a Tafel slope of 58 mV/dec), especially at large current density. Also, the mass activity of PtSe2/Pt and Pt/C are compared in Figure S5. This observation reveals that the outstanding activity of $PtSe_2/Pt$ does not originate totally from Pt, indicating new highly active sites other than Pt are generated. To further explore the nature of the observed high activity of $PtSe_2/Pt$, we measured the electrical double layer capacitances (C_{dl}) in Figure 3c. The value of C_{dl} is obtained by data processing of cyclic voltammetry at different scanning speeds, as shown in Figure S4. It is found that the electrochemical active area of $PtSe_2/Pt$ and $PtSe_2$ is similar to each other with 5.8 mF cm^{-2} for $PtSe_2/Pt$ and 4.9 mF cm^{-2} for $PtSe_2$, respectively, suggesting similar active sites loading. Therefore, the large improvement of the HER activity of $PtSe_2/Pt$ must be deduced from the upgrading of the activity of single site. The electrochemical impedance diagrams of $PtSe_2$ and $PtSe_2/Pt$ are shown in the up and down panels in Figure 3d, which can be fitted by the equivalent circuits. The electrochemical data is summarized in Table S2. As one can see, the electrical impedance of $PtSe_2/Pt$ is much smaller than $PtSe_2$, which implies the improved conductivity facilitates the superior activity of $PtSe_2/Pt$. The long-term stability test of $PtSe_2/Pt$ is shown in Figure 3e, which confirms the as-prepared $PtSe_2/Pt$ maintains its high low overpotential and shows good stability. The polarization curve after 1000 CV circles is illustrated in Figure S8, showing the same results. The Faraday efficiency of our sample was evaluated using a gas chromatography and a gas proof H-shaped electrolytic tank (Figure S6), with results listed in Figure S7. The XRD, TEM and XPS characterizations after stability test are shown in Figure S9, Figure S10 and Figure S11, respectively. It can be deduced that the $PtSe_2/Pt$ keeps its structure, morphology, crystal and oxidation state after the harsh stability test. The stability of $PtSe_2/Pt$ sample can be further confirmed by these characterizations. To emphasis the high performance of $PtSe_2/Pt$, a brief summarization of the Tafel slope and overpotential for various Pt-based or typical HER catalysts in alkaline electrolyte is shown in Figure 3f.

10.1002/anie.202110335

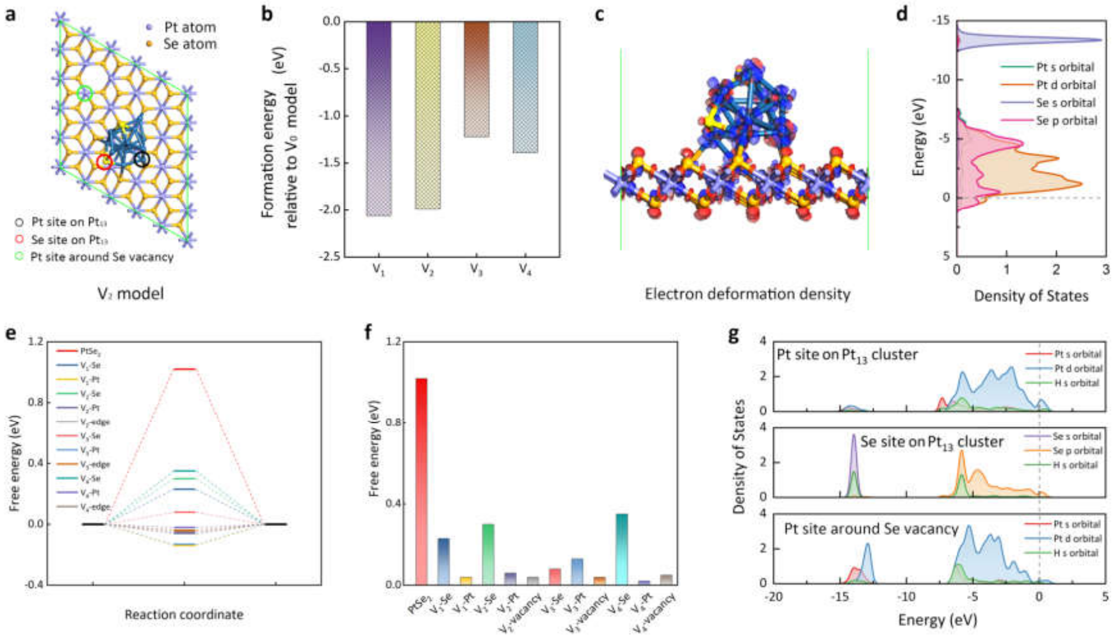

Figure 4. DFT calculations. **a** The structure model in the DFT calculation: $PtSe_2$ nanosheet decorated with Pt_{13} cluster. Colored circles mark the active centers. V_n means that n Se vacancies are included. **b** The formation energy relative to V_0 model. **c** Electron deformation density of the V_2 model. **d** Partial density of states of the V_2 model. **e** The H adsorption free energy of the active sites marked in a. **f** Absolute value of the H adsorption free energy. **g** The partial density of states between H and active sites of the V_2 model.

To investigate the underlying mechanism that triggers the activity enhancement, the density function theory (DFT) calculations are performed within an electrochemical framework to ascertain the HER activity of the functional $PtSe_2$/Pt material. Since Pt nanoparticle with a size of ~ 2 nm is nearly impossible for DFT calculations, the Pt_{13} cluster is adopted as the alternative in our present work. In the optimized structure, several Se atoms tend to transfer to the Pt_{13} cluster, leaving Se vacancies in the basal $PtSe_2$ nanosheet. This trend is in accord with the STEM observation. The stimulation models are descripted in Figure 4a and Figure S12, where V_n stands for the number of Se vacancies that are induced due to the Pt decoration. As illustrated in Figure 4b, the formation energy of V_n is clearly negative compared to the V_0 model (Table S3 for details), which thermodynamically accounts for the generation of Se vacancies. Moreover, strong Pt-Pt bonding between the cluster and the $PtSe_2$ substrate is formed to anchor the Pt cluster, which indicates high stability of this material. Additionally, Figure 4 c and Figure 4d character the electron deformation density and partial band structure of the reprehensive V_2 model, respectively. One can see the large overlap between the Pt 5*d* and Se 4*p* orbitals, as well as the dense electron cloud between the Pt cluster and $PtSe_2$ basal plane, which verifies again the generation of Se vacancies. Overall, these results indicate that the thermodynamic preference of Se vacancies stems from the strong covalent bonding of Pt-Se bonds.

According to the Sabatier principle, the ideal HER electrocatalyst should possess the subtle balance between H adsorption and the H protonation, which means that the universal descriptor, H adsorption free energy ΔG, features with the thermo-neutrality to represent the superior HER activity[15]. In the regard, Figure 4e provides the free energy profiles of the active centers and the absolute value of ΔG is summarized in Figure 4f. The ΔG of 1.02 eV clearly uncovers the insufficient proton adsorption on the Se site of the pristine $PtSe_2$, suggesting poor activity of pristine $PtSe_2$ nanosheet. By decorating Pt nanoparticles, the affinity of active H• species can be largely improved on the exposed Pt sites at the very vicinity of Se vacancies and the Pt/Se sites on the Pt cluster, delivering high HER activity. Taking V_2 model as an illustration, the corresponding ΔG are -0.04, 0.30 and -0.06 eV, respectively, some of which even outperforms the art-of-state Pt (ΔG = -0.09 eV). The similar tendencies are preserved for V_1 and V_3 models. The free energy values of various sites in the considered calculation models are summarized in Table S4. Figure 4g provides the density of states of the active centers to shed lights on the enhanced H adsorption. The Se-H bond originates from the *sp* hybridization while the Pt-H stems from the *sd* couplings, in line with the previous reports. What's more, to better mimic the ultra-small Pt particle, the Pt_{38} cluster models were also calculated with results shown in Figure S13, Table S3 and Table S4, which show the same trend with the Pt_{13} model. The theoretical data confirms the good HER activity of the advanced $PtSe_2$/Pt material.

3. Conclusions

In summary, we report large performance improvement on the HER activity of $PtSe_2$ nanosheet, a typical NMD compound. Ultra-small Pt nanoparticles are in situ generated on the edge of $PtSe_2$ nanosheet to form the $PtSe_2$/Pt heterointerface, with induced Se vacancies distributed along the boundary. The Se vacancies reduce the coordination environment, exposing highly active Pt centers. DFT calculations reveals that the free energy change can be optimized benefitting from this unique interface structure. The excellent HER activity is examined in alkaline electrolyte, with an overpotential of 42 mV at 10 mA/cm^2 and a Tafel slope of 53 mV/dec.

Acknowledgements

This study was supported by Key Research and Development of Ministry of Science and Technology of China (No. 2018YFE0202601), National Natural Science Foundation of China (51902220, 52072255) and Natural Science Foundation of Zhejiang Province (No. LY21E020001, LTY20E020001).

Conflict of Interest

The authors declare no conflict of interests regarding the publication of this article.

References

[1] L. Pi, L. Li, K. Liu, Q. Zhang, H. Li, T. Zhai, *Adv. Funct. Mater.* **2019**, *29*, 1904932; X. Yu, P. Yu, D. Wu, B. Singh, Q. Zeng, H. Lin, W. Zhou, J. Lin, K. Suenaga, Z. Liu, Q. J. Wang, *Nat. Commun.* **2018**, *9*, 1545; Y. Zhou, J. Zhang, E. Song, J. Lin, J. Zhou, K. Suenaga, W. Zhou, Z. Liu, J. Liu, J. Lou, H. J. Fan, *Nat. Commun.* **2020**, *11*, 2253.

[2] A. Politano, G. Chiarello, C.-N. Kuo, C. S. Lue, R. Edla, P. Torelli, V. Pellegrini, D. W. Boukhvalov, *Adv. Funct. Mater.* **2018**, *28*, 1706504; X. Chia, A. Adriano, P. Lazar, Z. Sofer, J. Luxa, M. Pumera, *Adv. Funct. Mater.* **2016**, *26*, 4306; J. Shi, X. Wang, S. Zhang, L. Xiao, Y. Huan, Y. Gong, Z. Zhang, Y. Li, X. Zhou, M. Hong, Q. Fang, Q. Zhang, X. Liu, L. Gu, Z. Liu, Y. Zhang, *Nat. Commun.* **2017**, *8*, 958; Q. Fu, J. Han, X. Wang, P. Xu, T. Yao, J. Zhong, W. Zhong, S. Liu, T. Gao, Z. Zhang, L. Xu, B. Song, *Adv. Mater.* **2021**, *33*, 1907818; Z. Lin, B. Xiao, Z. Wang, W. Tao, S. Shen, L. Huang, J. Zhang, F. Meng, Q. Zhang, L. Gu, W. Zhong, *Adv. Funct. Mater.* **2021**, *31*, 2102321.

[3] Z. Wang, Z. Lin, J. Deng, S. Shen, F. Meng, J. Zhang, Q. Zhang, W. Zhong, L. Gu, *Adv. Energy Mater.* **2020**, *11*, 202003023; M.-W. Gu, H. H. Peng, I. W. P. Chen, C.-h. Chen, *Nat. Mater.* **2021**, *20*, 658.

[4] D. Hu, T. Zhao, X. Ping, H. Zheng, L. Xing, X. Liu, J. Zheng, L. Sun, L. Gu, C. Tao, D. Wang, L. Jiao, *Angew. Chem. Int. Edit.* **2019**, *58*, 6977.

[5] S. Lin, Y. Liu, Z. Hu, W. Lu, C. H. Mak, L. Zeng, J. Zhao, Y. Li, F. Yan, Y. H. Tsang, X. Zhang, S. P. Lau, *Nano Energy* **2017**, *42*, 26.

[6] Z. Wang, Z. Lin, S. Shen, W. Zhong, S. Cao, *Chinese J. Catal.* **2021**, *42*, 710; F. Xu, K. Meng, B. Cheng, S. Wang, J. Xu, J. Yu, *Nat. Commun.* **2020**, *11*, 4613; C. Huang, Y. Wen, J. Ma, D. Dong, Y. Shen, S. Liu, H. Ma, Y. Zhang, *Nat. Commun.* **2021**, *12*, 320; W. Shin, J. Lu, X. Ji, *Carbon Energy* **2019**, *1*, 165.

[7] Y. Zhu, W. Peng, Y. Li, G. Zhang, F. Zhang, X. Fan, *J. Mater. Chem. A* **2019**, *7*, 23577; M. Kitamura, M. Kobayashi, E. Sakai, M. Minohara, R. Yukawa, D. Shiga, K. Amemiya, Y. Nonaka, G. Shibata, A. Fujimori, H. Fujioka, K. Horiba, H. Kumigashira, *Phys. Rev. B* **2019**, *100*, 245132;

S. Shen, Z. Lin, K. Song, Z. Wang, L. Huang, L. Yan, F. Meng, Q. Zhang, L. Gu, W. Zhong, *Angew. Chem. Int. Edit.* **2021**, *60*, 12360; J. Wu, Y. Cao, H. Zhao, J. Mao, Z. Guo, *Carbon Energy* **2019**, *1*, 57; S. Shen, R. Zhou, Y. Li, B. Liu, G. Pan, Q. Liu, Q. Xiong, X. Wang, X. Xia, J. Tu, *Small Methods* **2019**, *3*, 1900596.

[8] K. Zhang, B. Jin, Y. Gao, S. Zhang, H. Shin, H. Zeng, J. H. Park, *Small* **2019**, *15*, 1804903; Z. Lin, S. Shen, Z. Wang, W. Zhong, *iScience* **2021**, *24*, 102469.

[9] G. Zhao, K. Rui, S. X. Dou, W. Sun, *Adv. Funct. Mater.* **2018**, *28*, 1803291; W. Zhong, B. Xiao, Z. Lin, Z. Wang, L. Huang, S. Shen, Q. Zhang, L. Gu, *Adv. Mater.* **2021**, *33*, 2007894.

[10] J. Zhu, Y. Guo, F. Liu, H. Xu, L. Gong, W. Shi, D. Chen, P. Wang, Y. Yang, C. Zhang, J. Wu, J. Luo, S. Mu, *Angew. Chem. Int. Edit.* **2021**, *133*, 12436.

[11] M. A. Matin, E. Lee, H. Kim, W.-S. Yoon, Y.-U. Kwon, *J. Mater. Chem. A* **2015**, *3*, 17154; X. I. Pereira-Hernández, A. DeLaRiva, V. Muravev, D. Kunwar, H. Xiong, B. Sudduth, M. Engelhard, L. Kovarik, E. J. M. Hensen, Y. Wang, A. K. Datye, *Nat. Commun.* **2019**, *10*, 1358.

[12] J. H. Kim, J. Y. Cheon, T. J. Shin, J. Y. Park, S. H. Joo, *Carbon* **2016**, *101*, 449.

[13] R. Zhang, D. Drysdale, V. Koutsos, R. Cheung, *Adv. Funct. Mater.* **2017**, *27*, 1702455; X.-L. Zhang, S.-J. Hu, Y.-R. Zheng, R. Wu, F.-Y. Gao, P.-P. Yang, Z.-Z. Niu, C. Gu, X. Yu, X.-S. Zheng, C. Ma, X. Zheng, J.-F. Zhu, M.-R. Gao, S.-H. Yu, *Nat. Commun.* **2019**, *10*, 5338.

[14] K. Xu, H. Ding, M. Zhang, M. Chen, Z. Hao, L. Zhang, C. Wu, Y. Xie, *Adv. Mater.* **2017**, *29*, 1606980; L. Fu, Y. Li, N. Yao, F. Yang, G. Cheng, W. Luo, *ACS Catal.* **2020**, *10*, 7322; Y. Hong, C. H. Choi, S.-I. Choi, *ChemSusChem* **2019**, *12*, 4021; T. Liu, B. Feng, X. Wu, Y. Niu, W. Hu, C. M. Li, *ACS Applied Energy Materials* **2018**, *1*, 3143; M. Lao, K. Rui, G. Zhao, P. Cui, X. Zheng, S. X. Dou, W. Sun, *Angew. Chem. Int. Edit.* **2019**, *58*, 5432; R. Kavian, S.-I. Choi, J. Park, T. Liu, H.-C. Peng, N. Lu, J. Wang, M. J. Kim, Y. Xia, S. W. Lee, *J. Mater. Chem. A* **2016**, *4*, 12392; D. S. Baek, G. Y. Jung, B. Seo, J. C. Kim, H.-W. Lee, T. J. Shin, H. Y. Jeong, S. K. Kwak, S. H. Joo, *Adv. Funct. Mater.* **2019**, *29*, 1901217; H. Zhang, Y. Liu, H. Wu, W. Zhou, Z. Kou, S. J. Pennycook, J. Xie, C. Guan, J. Wang, *J. Mater. Chem. A* **2018**, *6*, 20214; Y. Wang, L. Chen, X. Yu, Y. Wang, G. Zheng, *Adv. Energy Mater.* **2017**, *7*, 1601390; F. Haque, A. Zavabeti, B. Y. Zhang, R. S. Datta, Y. Yin, Z. Yi, Y. Wang, N. Mahmood, N. Pillai, N. Syed, H. Khan, A. Jannat, N. Wang, N. Medhekar, K. Kalantar-zadeh, J. Z. Ou, *J. Mater. Chem. A* **2019**, *7*, 257; T. Kou, T. Smart, B. Yao, I. Chen, D. Thota, Y. Ping, Y. Li, *Adv. Energy Mater.* **2018**, *8*, 1703538.

[15] B. Hinnemann, P. G. Moses, J. Bonde, K. P. Jørgensen, J. H. Nielsen, S. Horch, I. Chorkendorff, J. K. Nørskov, *J. Am. Chem. Soc.* **2005**, *127*, 5308; D. Mukherjee, P. M. Austeria, S. Sampath, *ACS Energy Lett.* **2016**, *1*, 367; W. I. Choi, B. C. Wood, E. Schwegler, T. Ogitsu, *Adv. Energy Mater.* **2015**, *5*, 1501423; C. Tsai, F. Abild-Pedersen, J. K. Nørskov, *Nano Lett.* **2014**, *14*,

1381.